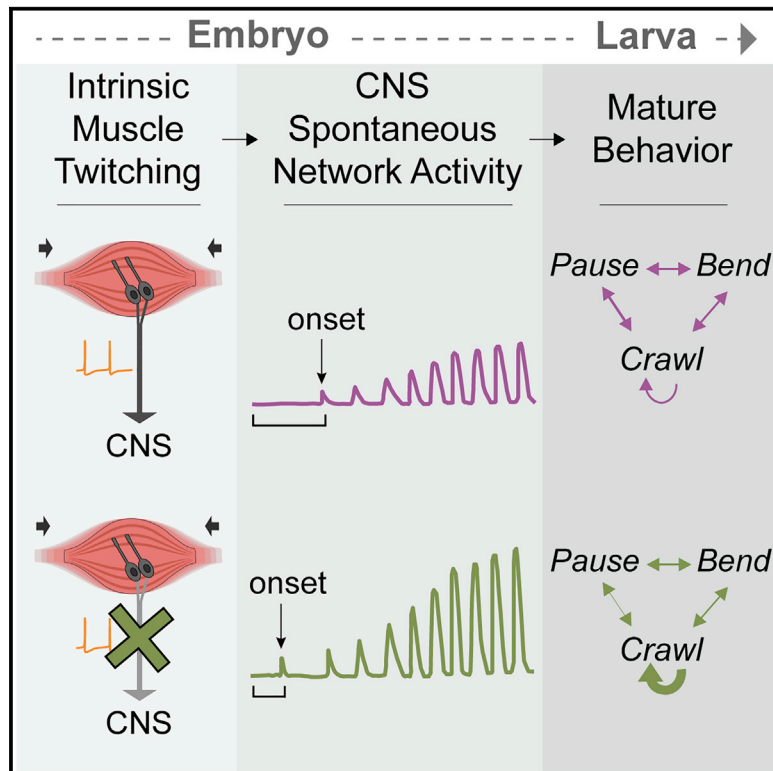# Current Biology

Mechanosensory input during circuit formation shapes *Drosophila* motor behavior through patterned spontaneous network activity

Graphical abstract

Authors

Arnaldo Carreira-Rosario,
Ryan A. York, Minseung Choi,
Chris Q. Doe, Thomas R. Clandinin

Correspondence

cdoe@uoregon.edu (C.Q.D.),
trc@stanford.edu (T.R.C.)

In brief

Carreira-Rosario et al. show that stereotyped, spontaneous network activity in the *Drosophila* embryo shapes innate larval behavior. This activity is negatively modulated by preceding intrinsic muscle twitching and sensory input. This work highlights self-generated sensory feedback as a mechanism to shape circuits that control innate behaviors.

Highlights

- PaSNA in the *Drosophila* embryonic CNS is spatiotemporally stereotyped

- Mechanosensory neurons negatively modulate PaSNA

- Embryonic PaSNA is required for innate locomotor behavior

CelPress

Current Biology

CellPress

Report

Mechanosensory input during circuit formation shapes *Drosophila* motor behavior through patterned spontaneous network activity

Arnaldo Carreira-Rosario,[1,2] Ryan A. York,[1] Minseung Choi,[1] Chris Q. Doe,[2,*] and Thomas R. Clandinin[1,3,*]
[1]Department of Neurobiology, Stanford University, Stanford, CA 94305, USA
[2]Institute of Neuroscience, Howard Hughes Medical Institute, University of Oregon, Eugene, OR 97403, USA
[3]Lead contact
*Correspondence: cdoe@uoregon.edu (C.Q.D.), trc@stanford.edu (T.R.C.)
https://doi.org/10.1016/j.cub.2021.08.022

SUMMARY

Neural activity sculpts circuit wiring in many animals. In vertebrates, patterned spontaneous network activity (PaSNA) generates sensory maps and establishes local circuits.[1–3] However, it remains unclear how PaSNA might shape neuronal circuits and behavior in invertebrates. Previous work in the developing *Drosophila* embryo discovered intrinsic muscle activity that did not require synaptic transmission, and hence was myogenic, preceding PaSNA.[4–6] These studies, however, monitored muscle movement, not neural activity, and were therefore unable to observe how myogenic activity might relate to subsequent neural network engagement. Here we use calcium imaging to directly record neural activity and characterize the emergence of PaSNA. We demonstrate that the spatiotemporal properties of PaSNA are highly stereotyped across embryos, arguing for genetic programming. Neural activity begins well before it becomes patterned, emerging during the myogenic stage. Remarkably, inhibition of mechanosensory input, as well as inhibition of muscle contractions, results in premature and excessive PaSNA, demonstrating that muscle movement serves as a brake on this process. Finally, transient mechanosensory inhibition during PaSNA, followed by quantitative modeling of larval behavior, shows that mechanosensory modulation during development is required for proper larval foraging. This work provides a foundation for using the *Drosophila* embryo to study the role of PaSNA in circuit formation, provides mechanistic insight into how PaSNA is entrained by motor activity, and demonstrates that spontaneous network activity is essential for locomotor behavior. These studies argue that sensory feedback during the earliest stages of circuit formation can sculpt locomotor behaviors through innate motor learning.

RESULTS

PaSNA in the *Drosophila* embryo

Motor movements begin in the embryo as uncoordinated twitching at stage 16, followed by larger scale movements that progressively become stronger and more organized prior to hatching approximately 7 h later (Figure 1A). To characterize the emergence of neural activity across these stages, we developed a wide-field imaging preparation in which we could monitor neural activity in 20–30 embryos simultaneously (Figure 1B; STAR Methods). We expressed the genetically encoded calcium indicator GCaMP6s in all neurons, while co-expressing nuclear TdTomato to allow for ratiometric imaging, and acquired images every 7 s from the myogenic stage through hatching (Video S1). Under these imaging conditions, 95% of control animals hatched (n = 60), demonstrating that this preparation does not disrupt normal development. Finally, to correct for small variations in the developmental timing of individual embryos, we monitored ventral nerve cord (VNC) condensation and normalized developmental stage by computing the ratio of the length of the embryo to the length

of the central nervous system (CNS) (Figure S1A), following standard methods.[7,8]

Consistent with the pattern of muscle movements,[5] we observed episodes in which intracellular calcium concentrations increased in many neurons and their neurites (Figures 1C and 1D; Video S1). Strikingly, the timing of the first large wave of neural activity was highly consistent from animal to animal, appearing at a length ratio of 2.2 (95% CI [0.06, 0.06]) (Figure S1B), corresponding to early stage 17. Aligning calcium traces by the timing of the first episode revealed that the overall patterned spontaneous network activity (PaSNA) pattern was qualitatively and quantitatively similar across all embryos (Figures 1D–1F). In particular, a total of 17 PaSNA episodes (95% CI [0.99, 0.99]) that occurred over 275 min (95% CI [18.3, 18.3]) preceded hatching (Figures S1B and S1C). Moreover, the size and duration of each wave of activity consistently increased over the first eight waves (Figure 1E). Finally, the interbout interval dramatically decreased over the first five episodes of PaSNA from 21.8 min (95% CI [2.3,2.5]) to 13.3 min (95% CI [1.1,1.2]) (Figure 1F). Stereotypy analysis revealed that the observed intervals were significantly more stereotyped across embryos than expected by
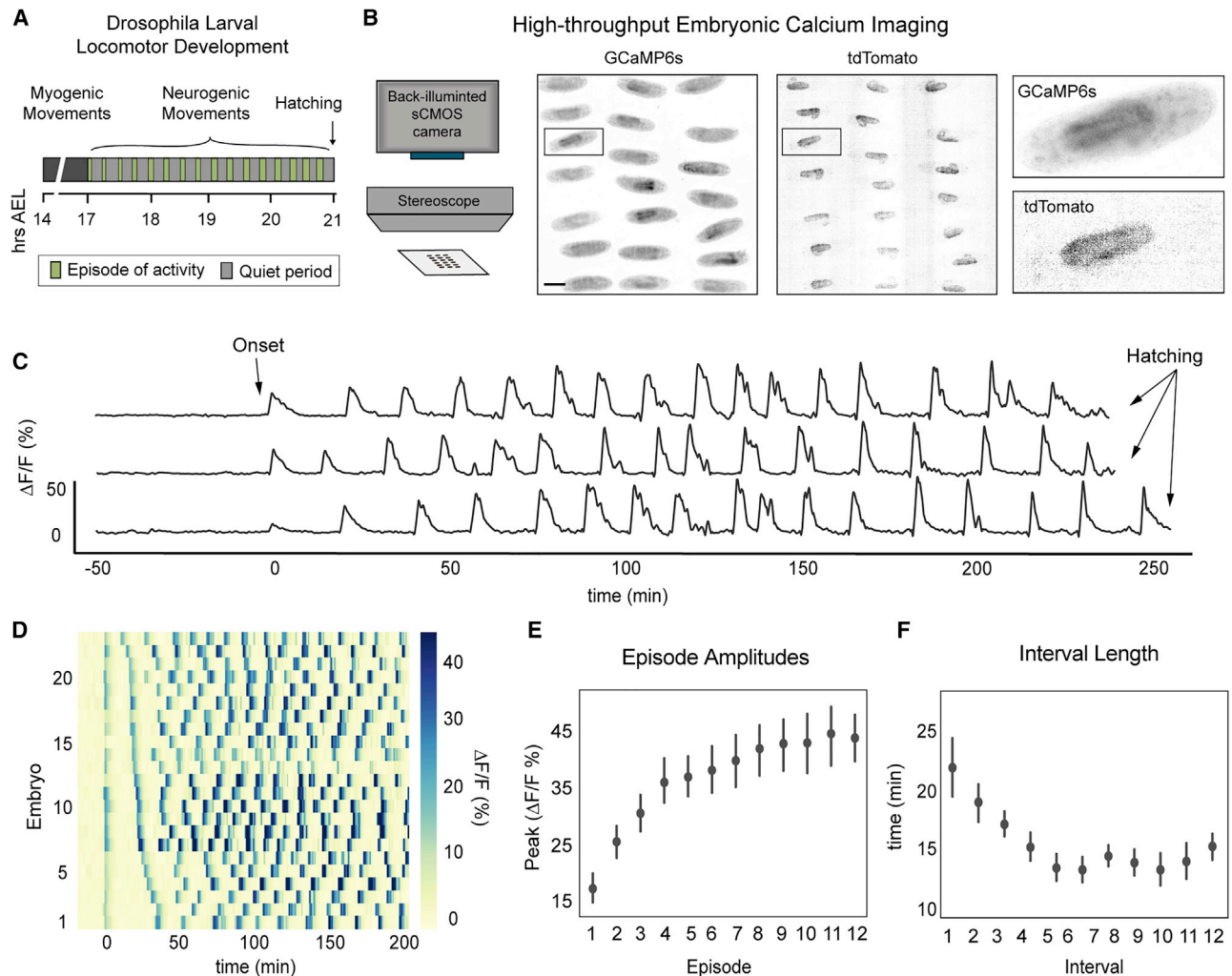
Figure 1. Characterization of patterned spontaneous network activity in the *Drosophila* embryo

(A) Schematic of *Drosophila* larval locomotor development. Time in hours after egg laying (hours AEL).

(B) Schematic of high-throughput imaging system (left). Images of GCaMP6s and tdTomato signal across the imaging field, color inverted for visualization (right). Scale bar, 200 μm.

(C) GCaMP6s:TdTomato ΔF/F traces from three individual embryos.

(D) Raster plot for PaSNA trimmed at 200 min post-onset, sorted by distance between first and second peak, with each trace corresponding to an individual embryo. Increasingly strong movements prevent accurate measurements at later stages. ΔF/F heatmap scale to the right.

(E) ΔF/F peaks for episodes 1 through 12 (n = 23).

(F) Quantification of the first eleven interbout interval lengths (n = 23).

For (E) and (F), points represent mean and lines depict the 95% confidence interval (CI).

See also Figure S1 and Video S1. For genotype information, see Table S1.

chance (Figure S1D). Taken together, these data show that PaSNA is highly stereotyped from embryo to embryo, suggesting that PaSNA is genetically encoded.

Spatiotemporal properties of the initial PaSNA episode

We focused next on the first episode of PaSNA, a period of particular interest given that it represents the transition from myogenic to neurogenic movement. To investigate the spatiotemporal patterns of neural activity during single episodes of PaSNA, we developed a two-photon (2P) microscopy preparation to image embryos expressing pan-neuronal GCaMP6s and TdTomato. This system allows for imaging of the VNC for 2 h

at cellular resolution, acquiring imaging volumes at 2.6 Hz. Embryos survive imaging, hatch, and become adult flies (n = 8). Preceding the first episode of PaSNA, we observed sporadic neuronal firing throughout the VNC, an activity pattern we refer to as flickering. This activity was observed during the 30 min before the first PaSNA episode, thus appearing during the myogenic phase of movement.[5] After this, the first PaSNA episode began and comprised three phases (Figures 2A and 2B; Video S2). During the first phase, we observed increased levels of neural activity within a stereotyped region, marking the localized initiation of PaSNA and defining the start of neurogenic activity. During the second phase, we observed a single

Current Biology

Report

🧬 **CellPress**
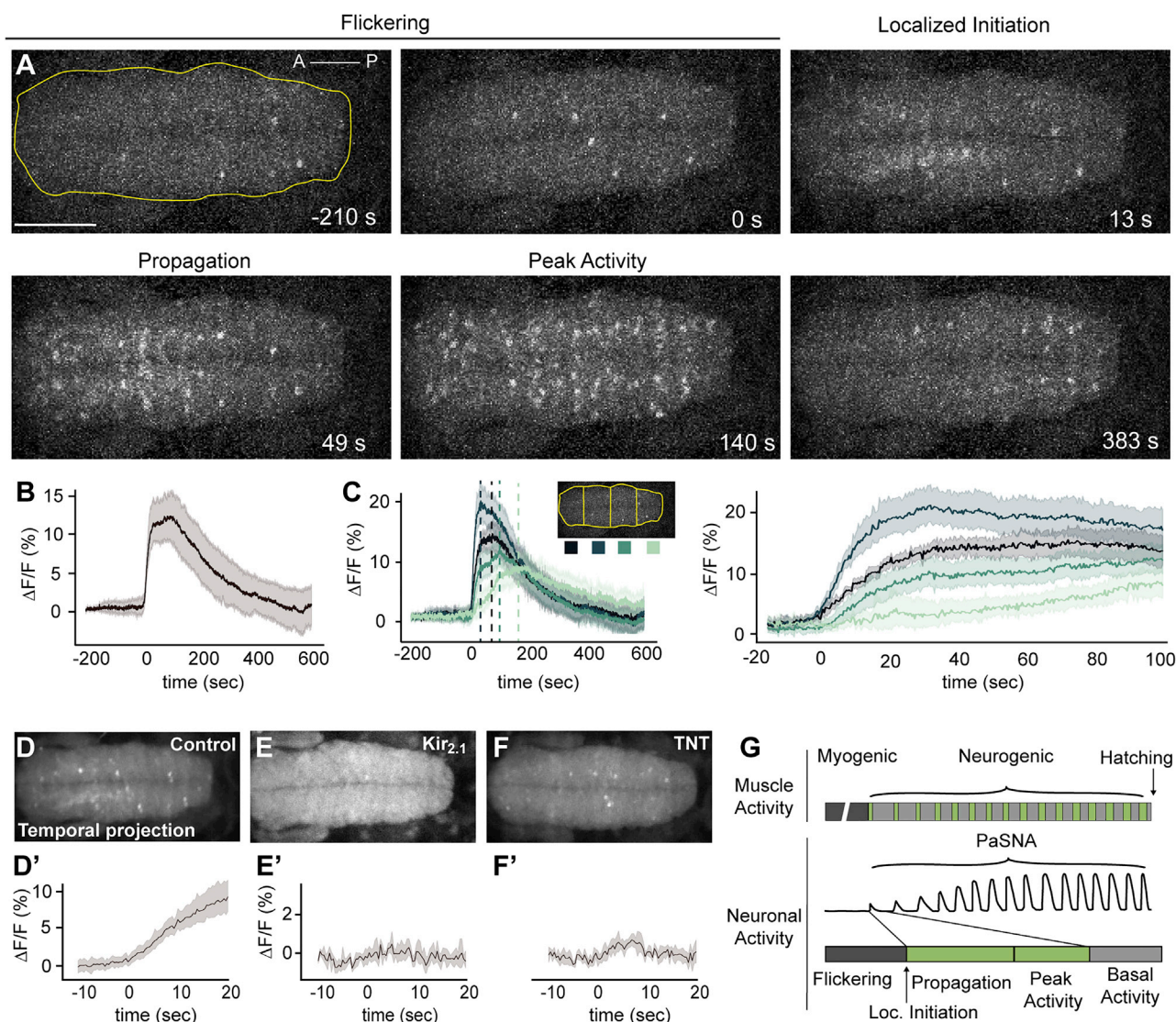
Figure 2. Spatiotemporal and network properties of a single PaSNA episode

(A) Image frames during the first episode of PaSNA in an embryo. Phases labeled on top. Images are maximum intensity projections from an embryonic VNC expressing pan-neuronal GCaMP6s. Time stamps are relative to the positive inflection point caused by the activity burst. Yellow line delineates the VNC, with the ROI used for (B). Scale bar, 50 μm.

(B) ΔF/F trace of the entire VNC during the first episode of PaSNA (n = 8).

(C) ΔF/F of the color-coded four ROIs. Left displays −200 s to 600 s; right displays from −20 to 100 s relative to the initiation of PaSNA.

(D–F) Temporal projections (top) and ΔF/F VNC traces (bottom) for 30 s near the localized initiation time of the episode for control embryos (n = 8) (D), embryos expressing Kir$_{2.1}$ pan-neuronally (E) (n = 5), and embryos expressing TNT pan-neuronally (F) (n = 6).

(G) Schematic of *Drosophila* larval locomotor development showing activity at the muscle (top) and neuronal (bottom) level. For all time series, dark lines represent the mean, while shading depicts the 95% CI.

See also Videos S2, S3, and S4. For genotype information, see Table S1.

wave of neural activity that traversed the VNC and defined propagation. During the third phase, we observed a period of peak activity along the VNC that persisted for approximately 80 s. Activity then returned to basal levels where an interbout interval containing flickering activity persisted until the next episode.

Next, we asked whether the location of the focal activity observed during localized initiation was invariant across embryos. Analysis of neural activity within ROIs along the anterior-posterior (A-P) axis of the VNC showed that PaSNA always

initiated in the anterior region of the VNC (Figure 2C) (n = 8). Furthermore, in 100% of embryos, activity initiated in one of the two most anterior ROIs, a region spanning the thoracic segments. After initiation, activity always propagated along the A-P axis. Strikingly, the wave of neural activity propagated slowly, reaching the most posterior region of the embryo approximately 75 s after localized initiation, corresponding to a propagation speed of less than 2 μm per second. Lastly, in all embryos, the more posterior regions were the last to return to basal, flickering
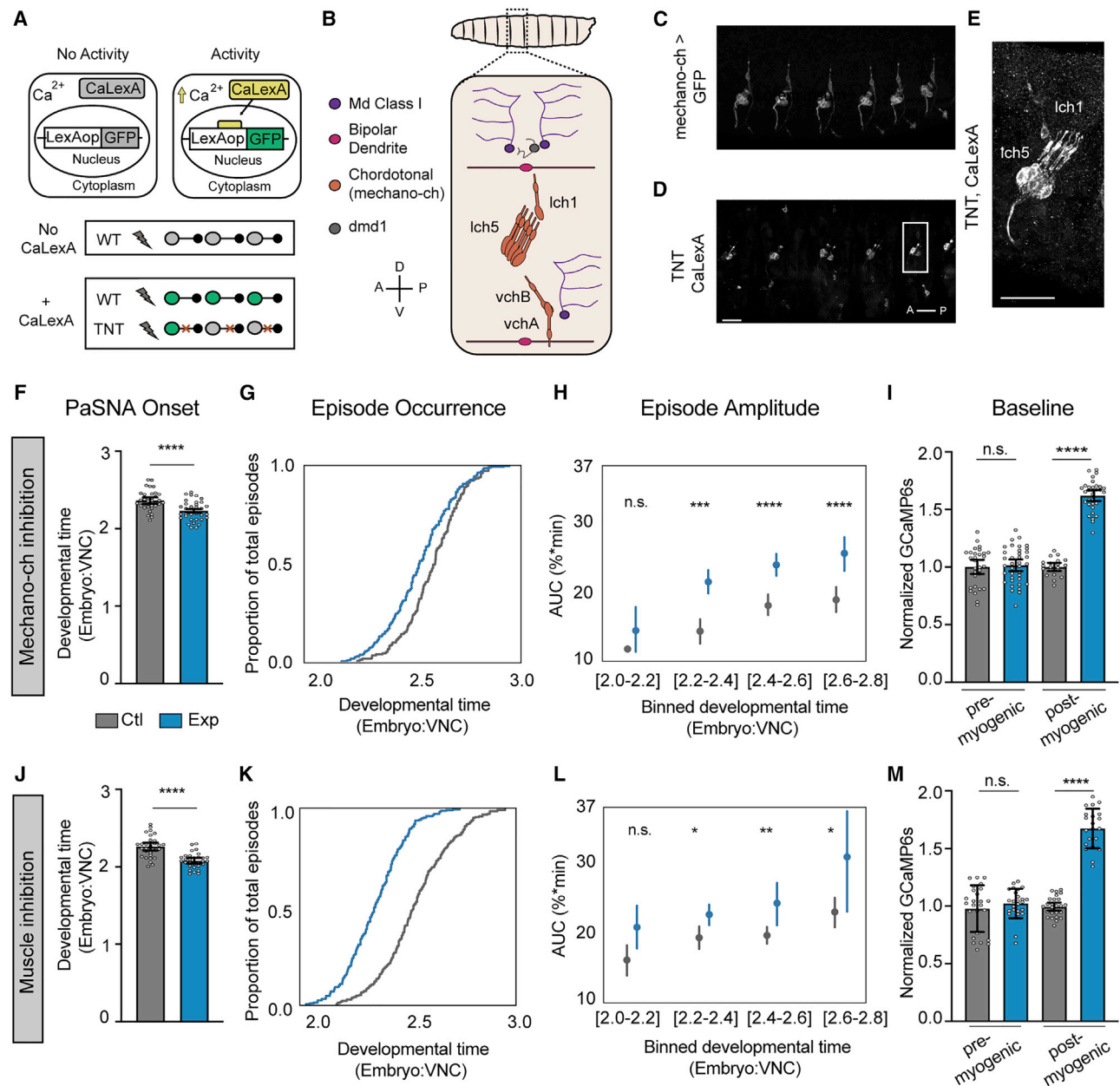
Figure 3. Mechanosensory neurons modulate the onset and amplitude of PaSNA episodes

(A) Schematic illustration of the experiment using CaLexA to reveal neural activity during the myogenic phase.

(B) Schematic of an embryonic anterior body wall hemisegment showing all proprioceptive neurons. There are eight mechanosensory chordotonal neurons (mechano-ch; orange). Five of these form a laterally located cluster (lch5). A solitary mechano-ch is located dorsal to lch5 (lch1), and a pair of mechano-ch neurons is located ventrally (vchB and vchA). Anatomical coordinates: anterior (A), posterior (P), dorsal (D), and ventral (V).

(C) Expression of the mechano-ch driver *inactive* (*iav*) along several body wall segments.

(D and E) CaLexA driving GFP expression in a 19 h AEL embryo expressing pan-neuronal TNT (n = 30 embryos). Note expression in lch5 in every hemisegment as well as expression in lch1 and vchA/B in some segments. Scale bars, 20 μm.

(F–I) Measurements of the timing and intensity of PaSNA in control embryos (gray) and experimental embryos expressing TNT in mechano-ch neurons (blue).

(F) Quantification of PaSNA onset (n = 36 control; n = 33 experimental).

(G) Cumulative occurrence of the first twelve episodes plotted as the proportion of total episodes across developmental time (n = 17 control; n = 32 experimental).

(H) Area under the peak curve (AUC) quantification for the first twelve episodes plotted against developmental time. Values were binned based on developmental time (n = 17 control; n = 32 experimental).

(I) Quantification of GCaMP6s baseline levels normalized against control mean before (14 h AEL; n = 30 control; n = 37 experimental) and after (10 min before PaSNA onset; n = 20 control; n = 32 experimental) the myogenic phase.

(J–M) Measurements of the timing and intensity of PaSNA in control embryos (gray) and experimental embryos expressing Kir$_{2.1}$ in muscles (blue).

(J) Quantification of PaSNA onset (n = 36 control; n = 30 experimental).

(legend continued on next page)

Current Biology
Report

activity. Together, these observations demonstrate that the initial episode of PaSNA is spatiotemporally patterned.

The role of neural activity in initiating PaSNA

Next, we examined the role of neural activity in the initiation of PaSNA. To test whether neuronal depolarization caused the observed calcium transients, we inhibited depolarization through pan-neuronal expression of the inward-rectifier potassium channel $Kir_{2.1}$.[9] As expected, this abolished flickering during the myogenic phase, as well as all three phases of PaSNA, indicating that PaSNA is a voltage-dependent process (Figure 2E; Video S3). Next, we tested whether PaSNA is driven by chemical synapses by inhibiting synaptic transmission using tetanus toxin (TNT).[9] Pan-neuronal expression of TNT had no effect on flickering during the myogenic phase but prevented all three phases of PaSNA including the propagating waves of neural activity (Figure 2F; Video S4). Together, these results show that while neuronal depolarization and chemical synaptic transmission are both crucial for PaSNA, only depolarization is required for flickering.

Mechanosensory input negatively modulates PaSNA

We next sought to determine whether the initial, myogenic phase of spontaneous muscle movement might be functionally coupled to the initiation of PaSNA. We reasoned that this coupling could occur through sensory feedback via proprioceptors. Therefore, we first asked which proprioceptive neurons are active during the myogenic phase. We used the calcium integrator system CaLexA, a method for transcriptionally labeling active neurons (Figure 3A).[10] We restricted this system to only those neurons that are active during the myogenic phase by pan-neuronal expression of TNT, which prevents embryos from entering PaSNA (Figures 2F and 3A). Strikingly, every embryo displayed high levels of CaLexA expression in mechanosensory chordotonal (mechano-ch) neurons in most segments (n = 30 embryos) (Figures 3B–3E). Specifically, we observed expression in lch5 in every hemisegment as well as expression in lch1 and vchA/B in some segments. Notably, none of these embryos showed CaLexA signal in any other proprioceptive neurons.

Mechano-ch neurons detect muscle stretch, relaying proprioceptive signals used to regulate larval crawling speed.[11–14] Additionally, these neurons have been previously linked to embryonic neural circuit formation,[12] making them ideal candidates for coupling muscle movements to PaSNA. To test this idea, we silenced mechano-ch neurons and examined whether this perturbation altered the timing or amplitude of PaSNA episodes. To do this, we used the *inactive (iav)* enhancer to express TNT in mechano-ch neurons and monitored neural activity throughout PaSNA using wide-field imaging of pan-neuronally expressed GCaMP6s. Consistent with previous work,[5] PaSNA was not abolished after mechano-ch silencing. Strikingly, however, PaSNA started prematurely in these embryos (Figure 3F). This led to embryos experiencing more episodes of PaSNA earlier in development (Figure 3G), as well as increasing PaSNA duration and the total number of episodes (Figures S2A and S2B). The amplitude of most PaSNA episodes was increased in these embryos as compared to controls (Figure 3H). Lastly, interbout intervals remained largely unchanged (Figure S2C).

We reasoned that if mechano-ch neurons were coupling muscle contraction to PaSNA, there might be an effect of blocking the synaptic transmission in these cells during the myogenic phase. To test this, we examined the baseline fluorescence of GCaMP6s (relative to nuclear TdTomato expressed on the same RNA transcript), as a proxy for the intracellular calcium concentration and membrane excitability, before and after the myogenic phase. As expected, inhibiting mechano-ch neurons had no effect on baseline fluorescence when muscles had not yet contracted, before the myogenic phase (Figure 3I). Strikingly, inhibiting mechano-ch neurons dramatically increased the baseline fluorescence signal of GCaMP6s after muscle contraction during the myogenic phase (but before PaSNA began; Figure 3I). Such an increase in baseline GCaMP6s signal is consistent with higher intracellular calcium concentrations and increased membrane excitability, providing a potential explanation for the premature onset and increased amplitude of PaSNA seen when mechano-ch neurons are inhibited. We note that this change in baseline GCaMP6s fluorescence cannot be accounted for by changes in protein expression, as these measures are normalized relative to TdTomato in every cell. Thus, mechano-ch neurons act during the myogenic phase. Finally, to complement these results, we repeated these experiments in embryos expressing $Kir_{2.1}$ in mechano-ch neurons. However, while we observed significant increases in the amplitudes of initial PaSNA episodes and GCaMP baseline (Figure S2G), overall effects were modest, suggesting that this functional inhibition was incomplete and further obscured by genetic background effects that increased baseline GCaMP6s fluorescence (Figure S2L).

If mechano-ch neurons are coupling muscle movements to PaSNA, inhibiting muscle contractions should have similar effects to inhibiting mechano-ch neurons. To test this, we inhibited muscle contraction by expressing $Kir_{2.1}$ using a muscle-specific driver,[15] while expressing GCaMP6s pan-neuronally. Strikingly, preventing muscle contraction caused premature PaSNA onset, increased the amplitude of PaSNA episodes, and led to higher baseline fluorescence in post-myogenic, but not pre-myogenic, embryos (Figures 3J–3M). Thus, silencing muscle contraction or proprioceptive neuron function leads to premature onset of PaSNA and increased amplitude of PaSNA episodes, strongly suggesting that muscle contractions induce mechano-ch activity during the myogenic phase to negatively modulate PaSNA.

(K) Cumulative occurrence of the first twelve episodes plotted as the proportion of total episodes across developmental time (n = 28 control; n = 28 experimental).
(L) AUC quantification for the first twelve episodes plotted against binned developmental time (n = 28 control; n = 28 experimental).
(M) Quantification of GCaMP6s baseline levels normalized against control mean before (n = 25 control; n = 25 experimental) and after (n = 26 control; n = 21 experimental) the myogenic phase.
For (H) and (L), points represent mean and lines depict the 95% CI. For all bar graphs, the mean and 95% CI are displayed. ****$p < 0.0001$, ***$p < 0.001$, **$p < 0.005$, *$p < 0.05$. For (F) and (J), we used two-sample t tests. For (H) and (L), we used two-sample t tests with Holm-Bonferroni correction. For (I) and (M), we used two-sample Welch's t tests to account for differences in variance.
See also Figure S2. For genotype information, see Table S1.
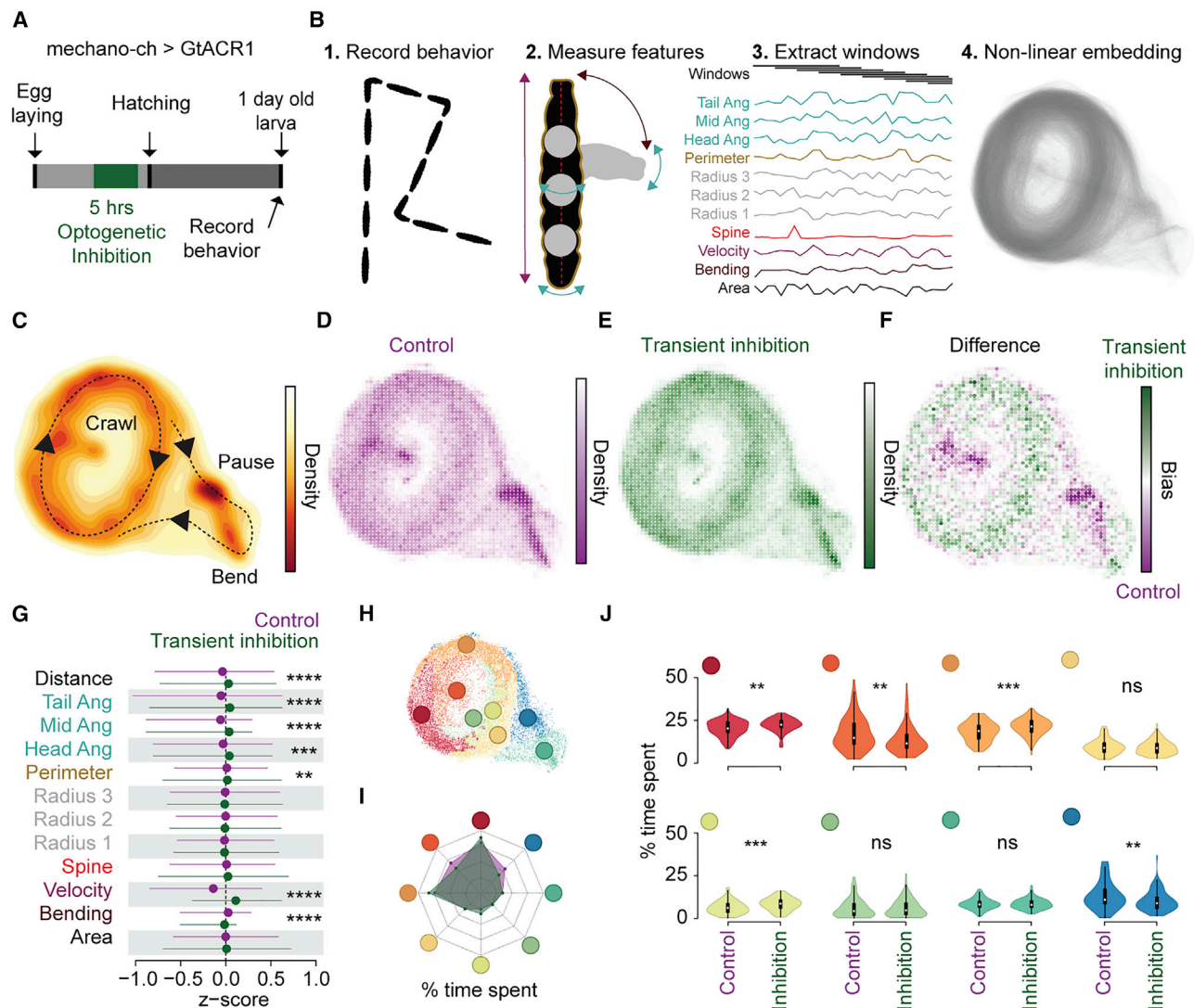
Figure 4. Temporal embryonic inhibition of mechanosensory input leads to abnormal larval behavior

(A) Schematic of experimental design.

(B) Workflow for time-resolved behavioral embedding (TREBLE) (STAR Methods).

(C) Probability density function of larval locomotor space plotted as a heatmap. Behaviors annotated qualitatively. Density scale to the right.

(D and E) Bin-wise occurrence distributions for control (n = 84) (D) and transient inhibition (n = 97) (E) groups.

(F) Difference map between control (purple) and transiently inhibited (green) animals. Bias scale to the right.

(G) Comparison of primary behavioral features between control (purple) and transiently inhibited (green) larvae.

(H) Behavioral space colored via Louvain clusters (STAR Methods).

(I) Radar chart comparing the percentage of time spent in each of the Louvain clusters for control (purple) and transient inhibition (green) groups.

(J) Differences in occurrence in each behavioral cluster between control and transiently inhibited animals.

****p < 0.0001, ***p < 0.001, **p < 0.01. For (G), we used trial-wise Kruskal-Wallis test with Bonferroni correction. For (J), we used trial-wise Kruskal-Wallis test. See also Figure S3. For genotype information, see Table S1.

Developmental inhibition of mechanosensory input leads to abnormal larval behavior

Our observation that silencing mechano-ch neurons increased PaSNA raised the question of whether this change in PaSNA had behavioral consequences, and more specifically, whether these transient changes in PaSNA resulted in larval behavioral deficits. We inhibited mechano-ch activity transiently (from the late myogenic phase through to the end of PaSNA) by expressing the *G. theta* anion channelrhodopsin 1 (GtACR1)[16] in mechano-

ch neurons and examined larval behavior 24 h after hatching using the frustrated total internal reflection-based imaging method (FIM; Figure 4A).[17] We employed time-resolved behavioral embedding (TREBLE)[18] to characterize potential behavioral differences between the optogenetically silenced condition and the control. TREBLE is a quantitative framework for identifying structure in behavior by collecting features (such as larval posture or velocity) into temporal windows and embedding these into a low-dimensional space (Figure 4B). As previously shown,[18]

Current Biology
Report

CellPress

we found that the major components of the larval foraging etho-gram[19,20] can be captured in a two-dimensional space using TREBLE (Figures 4B and 4C). In this two-dimensional space, crawling is represented by an oscillator with directional movement (Figure S3) and is connected to regions corresponding to pausing and turning (Figure 4C).

In the TREBLE approach, both control and transiently inhibited larvae were used to generate a single, common behavior space (n = 181 total; 84 control larvae, 97 transiently inhibited larvae; 179,409 windows; STAR Methods) where we could directly infer behavioral variation via differences in the likelihood that either control or experimental larvae occupied specific regions of the space (Figures 4D and 4E). Control and inhibited conditions displayed notably different occurrence distributions (Figures 4D–4F), the biggest deviations of which were restricted to specific regions of behavior space (Figure 4F). Control larvae were more likely to visit parts of the behavior space that correspond to pauses and bends (Figures 4F and S3) while inhibited larvae spent more time, proportionally, in the crawling oscillator (Figure 4F). To confirm these differences using a TREBLE-independent approach, we compared the primary behavioral features themselves, as measured using the FIM system, and observed that inhibited larvae bend less, crawl further, and have an increased velocity distribution relative to control animals (Figure 4G).

Finally, to quantitatively compare control and transiently inhibited larvae in the TREBLE space, we clustered the behavior space based on similarity to identify discrete elements of behavior (STAR Methods). We then compared the frequency of occurrence of discrete behavioral motifs (Figure 4H). Reflecting our previous findings, the mechano-ch silenced and control animals displayed different overall distributions (Figure 4I) and significantly varied across a number of behavioral motifs (Figure 4J; trial-wise Kruskal-Wallis test). Specifically, controls were more likely to pause (Figure 4J; dark blue; p < 0.01) and head cast during crawling (Figure 4J; dark orange; p < 0.002) while the mechano-ch silenced larvae were more likely to be crawling (Figure 4J; red, orange, light green). These findings demonstrate that developmental inhibition of mechano-ch neurons leads to an apparent simplification of larval foraging behavior, biasing animals toward ongoing crawling as opposed to the typical sequence of crawling, pausing, and head casting.

DISCUSSION

These studies demonstrate that PaSNA in the *Drosophila* embryo follows a stereotyped sequence of wave-like, large-scale network activation events interspersed by low-activity periods (Figures 1 and 2). Strikingly, our data also demonstrate that muscle contractions shape the magnitude of PaSNA via mechanosensory input, beginning during the myogenic phase, but perhaps also continuing throughout each subsequent wave (Figure 3). Transiently disrupting this mechanosensory feedback during embryonic development results in deficits in larval loco-motor behavior, arguing that neural activity plays a critical role in the functional organization of locomotor circuits (Figure 4). These results suggest that sensory inputs generated by spontaneous muscle contraction play a role in subsequent circuit establishment, thereby providing one of the earliest examples of sensory regulation of locomotor development in any context.

Our work has measured the trajectory of neural activity across embryonic development. Prior to PaSNA, individual CNS neurons display transient elevations in intracellular calcium levels (flickering) that depend on depolarization of the plasma membrane, but that are independent of synaptic input. In addition, as previous work has demonstrated, muscle twitching independent of neural activity also occurs and, based on our work, appears to lead to the selective activation of mechano-ch sensory neurons. The output of mechano-ch neurons then acts to negatively modulate the basal levels of intracellular calcium in the CNS, the onset of PaSNA, and the amplitude of PaSNA waves. While it is possible that the activation of mechano-ch neurons occurs independently of muscle contraction, given the phenotypic similarities revealed by muscle inhibition and mechano-ch inhibition (Figure 3), we favor a model where mechano-ch neuronal activity is driven by muscle contraction.

Our data demonstrate that the first episode of PaSNA invariably begins in the thoracic region (Figure 2). After this initial event, PaSNA proceeds through a stereotyped sequence of accelerating, intensifying waves through to hatching. Given the striking similarity in both the spatial and temporal properties of PaSNA in the embryo, as well as analogous observations in the *Drosophila* visual system,[21] we hypothesize that this process is under tight genetic control. Similarly, observations across systems, including in the mammalian cortex, have led to speculation that genetic information underlies the spontaneous neuronal activity present in these developing circuits.[22] Our characterization of the initiation and progression of PaSNA in the *Drosophila* embryo sets the stage for the dissection of these mechanisms at the level of specific circuits, cells, and molecules.

Most previous studies examining PaSNA function in shaping developing circuits rely on perturbations that abolish PaSNA. Interestingly, our study shows that an increase in PaSNA also leads to changes in behavior. This result suggests that organisms must quantitatively tune the level of PaSNA during circuit establishment. Supporting this, previous studies have demonstrated that excessive neuronal activity during larval circuit formation leads to hyperexcitable motor circuits that are prone to seizures.[23,24] It is possible that the excessive PaSNA experienced after mechano-ch inhibition leads to hyperexcitability of specific neurons within the circuits that control foraging behavior. Identifying the neurons affected upon mechano-ch transient inhibition and probing their electrophysiological properties will test this idea.

Relatively little attention has been paid to examining the role of spontaneous neural activity in shaping innate behaviors. In that light, our finding that the activity of mechano-ch neurons during development shapes locomotor behavior is remarkable. Given that this behavioral effect is developmentally programmed, we hypothesize that mechano-ch input is needed to pattern connectivity or determine the physiological properties of specific cells in developing motor circuits. Indeed, blocking synaptic transmission in mechano-ch neurons throughout development changes the connectivity of these cells with their post-synaptic partners, cells that mediate behavioral responses to vibration.[25] We hypothesize that the changes that mechano-ch inputs exert on developing circuits are, in fact, widespread, modifying circuits across the CNS through PaSNA. In vertebrates, motor feedback is crucial to shaping learned motor behaviors through

CellPress

Current Biology
Report

activity-dependent mechanisms.[26] It is tempting to speculate that the sculpting of innate foraging behavior by mechano-ch neuron activity in *Drosophila* reveals an analogous, evolutionarily ancient mechanism that may have been co-opted in other contexts to enable motor learning.

STAR★METHODS

Detailed methods are provided in the online version of this paper and include the following:

- KEY RESOURCES TABLE
- RESOURCE AVAILABILITY
  - Lead contact
  - Materials availability
  - Data and code availability
- EXPERIMENTAL MODEL AND SUBJECT DETAILS
  - *Drosophila* Stocks
- METHOD DETAILS
  - Embryo collection for calcium imaging
  - Wide-field imaging
  - Two-photon imaging
  - Immunostaining and confocal imaging
  - Behavior data collection
- QUANTIFICATION AND STATISTICAL ANALYSIS
  - Processing of calcium imaging data
  - Episode and peak detection
  - Stereotypy of episode timing
  - Statistical analysis
  - Behavioral analysis

SUPPLEMENTAL INFORMATION

Supplemental information can be found online at https://doi.org/10.1016/j.cub.2021.08.022.

ACKNOWLEDGMENTS

AUTHOR CONTRIBUTIONS

DECLARATION OF INTERESTS

The authors declare no competing interests.

REFERENCES

1. Goodman, C.S., and Shatz, C.J. (1993). Developmental mechanisms that generate precise patterns of neuronal connectivity. Cell *72 (Suppl)*, 77–98.

2. Kirkby, L.A., Sack, G.S., Firl, A., and Feller, M.B. (2013). A role for correlated spontaneous activity in the assembly of neural circuits. Neuron *80*, 1129–1144.

3. Thompson, A., Gribizis, A., Chen, C., and Crair, M.C. (2017). Activity-dependent development of visual receptive fields. Curr. Opin. Neurobiol. *42*, 136–143.

4. Pereanu, W., Spindler, S., Im, E., Buu, N., and Hartenstein, V. (2007). The emergence of patterned movement during late embryogenesis of Drosophila. Dev. Neurobiol. *67*, 1669–1685.

5. Crisp, S., Evers, J.F., Fiala, A., and Bate, M. (2008). The development of motor coordination in Drosophila embryos. Development *135*, 3707–3717.

6. Crisp, S.J., Evers, J.F., and Bate, M. (2011). Endogenous patterns of activity are required for the maturation of a motor network. J. Neurosci. *31*, 10445–10450.

7. Campos-Ortega, J.A., and Hartenstein, V. (2013). The Embryonic Development of Drosophila melanogaster (Springer Science & Business Media).

8. Olofsson, B., and Page, D.T. (2005). Condensation of the central nervous system in embryonic Drosophila is inhibited by blocking hemocyte migration or neural activity. Dev. Biol. *279*, 233–243.

9. Baines, R.A., Uhler, J.P., Thompson, A., Sweeney, S.T., and Bate, M. (2001). Altered electrical properties in Drosophila neurons developing without synaptic transmission. J. Neurosci. *21*, 1523–1531.

10. Masuyama, K., Zhang, Y., Rao, Y., and Wang, J.W. (2012). Mapping neural circuits with activity-dependent nuclear import of a transcription factor. J. Neurogenet. *26*, 89–102.

11. Hehlert, P., Zhang, W., and Göpfert, M.C. (2021). Drosophila mechanosensory transduction. Trends Neurosci. *44*, 323–335.

12. Fushiki, A., Kohsaka, H., and Nose, A. (2013). Role of sensory experience in functional development of Drosophila motor circuits. PLoS ONE *8*, e62199.

13. Caldwell, J.C., Miller, M.M., Wing, S., Soll, D.R., and Eberl, D.F. (2003). Dynamic analysis of larval locomotion in Drosophila chordotonal organ mutants. Proc. Natl. Acad. Sci. USA *100*, 16053–16058.

14. Cheng, L.E., Song, W., Looger, L.L., Jan, L.Y., and Jan, Y.N. (2010). The role of the TRP channel NompC in Drosophila larval and adult locomotion. Neuron *67*, 373–380.

15. Zarin, A.A., Mark, B., Cardona, A., Litwin-Kumar, A., and Doe, C.Q. (2019). A multilayer circuit architecture for the generation of distinct locomotor behaviors in *Drosophila*. eLife *8*, e51781.

16. Mohammad, F., Stewart, J.C., Ott, S., Chlebikova, K., Chua, J.Y., Koh, T.-W., Ho, J., and Claridge-Chang, A. (2017). Optogenetic inhibition of behavior with anion channelrhodopsins. Nat. Methods *14*, 271–274.

17. Risse, B., Thomas, S., Otto, N., Löpmeier, T., Valkov, D., Jiang, X., and Klämbt, C. (2013). FIM, a novel FTIR-based imaging method for high throughput locomotion analysis. PLoS ONE *8*, e53963.

18. York, R.A., Carreira-Rosario, A., Giocomo, L.M., and Clandinin, T.R. (2021). Flexible analysis of animal behavior via time-resolved manifold embedding. bioRxiv. https://doi.org/10.1101/2020.09.30.321406.

19. Green, C.H., Burnet, B., and Connolly, K.J. (1983). Organization and patterns of inter- and intraspecific variation in the behaviour of Drosophila larvae. Anim. Behav. *31*, 282–291.

20. Clark, M.Q., McCumsey, S.J., Lopez-Darwin, S., Heckscher, E.S., and Doe, C.Q. (2016). Functional genetic screen to identify interneurons

Current Biology
Report

governing behaviorally distinct aspects of Drosophila larval motor programs. G3 (Bethesda) *6*, 2023–2031.

21. Akin, O., Bajar, B.T., Keles, M.F., Frye, M.A., and Zipursky, S.L. (2019). Cell-type-specific patterned stimulus-independent neuronal activity in the Drosophila visual system during synapse formation. Neuron *101*, 894–904.e5.

22. Khazipov, R., and Luhmann, H.J. (2006). Early patterns of electrical activity in the developing cerebral cortex of humans and rodents. Trends Neurosci. *29*, 414–418.

23. Giachello, C.N.G., and Baines, R.A. (2015). Inappropriate neural activity during a sensitive period in embryogenesis results in persistent seizure-like behavior. Curr. Biol. *25*, 2964–2968.

24. Giachello, C.N.G., and Baines, R.A. (2017). Regulation of motoneuron excitability and the setting of homeostatic limits. Curr. Opin. Neurobiol. *43*, 1–6.

25. Valdes-Aleman, J., Fetter, R.D., Sales, E.C., Heckman, E.L., Venkatasubramanian, L., Doe, C.Q., Landgraf, M., Cardona, A., and Zlatic, M. (2021). Comparative connectomics reveals how partner identity, location, and activity specify synaptic connectivity in Drosophila. Neuron *109*, 105–122.e7.

26. Makino, H., Hwang, E.J., Hedrick, N.G., and Komiyama, T. (2016). Circuit mechanisms of sensorimotor learning. Neuron *92*, 705–721.

27. Feng, K., Palfreyman, M.T., Häsemeyer, M., Talsma, A., and Dickson, B.J. (2014). Ascending SAG neurons control sexual receptivity of Drosophila females. Neuron *83*, 135–148.

28. Sen, R., Wang, K., and Dickson, B.J. (2019). TwoLumps ascending neurons mediate touch-evoked reversal of walking direction in Drosophila. Curr. Biol. *29*, 4337–4344.e5.

29. Shirangi, T.R., Stern, D.L., and Truman, J.W. (2013). Motor control of Drosophila courtship song. Cell Rep. *5*, 678–686.

30. Shearin, H.K., Dvarishkis, A.R., Kozeluh, C.D., and Stowers, R.S. (2013). Expansion of the gateway multisite recombination cloning toolkit. PLoS ONE *8*, e77724.

31. Manning, L., and Doe, C.Q. (2017). Immunofluorescent antibody staining of intact Drosophila larvae. Nat. Protoc. *12*, 1–14.

32. Risse, B., Berh, D., Otto, N., Klämbt, C., and Jiang, X. (2017). FIMTrack: an open source tracking and locomotion analysis software for small animals. PLoS Comput. Biol. *13*, e1005530.

33. Risse, B., Otto, N., Berh, D., Jiang, X., and Klämbt, C. (2014). FIM imaging and FIMtrack: two new tools allowing high-throughput and cost effective locomotion analysis. J. Vis. Exp. (94)

34. McInnes, L., Healy, J., and Melville, J. (2018). UMAP: uniform manifold approximation and projection for dimension reduction. arXiv, arXiv:1802.03426. https://arxiv.org/abs/1802.03426.

35. Csardi, G., and Nepusz, T. (2006). The igraph software package for complex network research. https://igraph.org.

STAR★METHODS

KEY RESOURCES TABLE

REAGENT or RESOURCE	SOURCE	IDENTIFIER
Antibodies		
Chicken anti-GFP	Abcam	Cat # ab13970; RRID:AB_300798
Anti-chicken Alexa 488	ThermoFisher	A-11039; RRID:AB_142924
Chemicals, peptides, and recombinant proteins		
All-trans-retinal	Sigma-Aldrich	R2500-100MG
Deposited data		
PaSNA data	This paper	https://github.com/ClandininLab/pasna-acr-currbio2021
Experimental models: Organisms/strains		
UAS-IVS-Syn21-GCaMP6s-P2A-nls-tdTomato-p10 (JK66B)	Gift from Marta Zlatic	N/A
LexAop- Kir$_{2.1}$ (VIE-260B)	Gift from Barry Dickson	Feng et al.[27]
UAS- Kir$_{2.1}$ (VIE-260B)	Gift from Barry Dickson	Feng et al.[27]
LexAop-TNT (VIE-260B)	Gift from Barry Dickson	Sen et al.[28]
pBDP-LexA:p65 (attp40)	Gift from Troy Shirangi	Shirangi et al.[29]
UAS-GtACR1(attP2)	Gift from Adam Claridge-Chang	Mohammad et al.[16]
elav-GAL4.L on 3rd	Bloomington Drosophila Stock Center	BDSC 8760
elav-GAL4.L on 2nd	Bloomington Drosophila Stock Center	BDSC 8765
GMR44H10-lexa::p65 (attP40)	Bloomington Drosophila Stock Center	BDSC 61543
elav^{c155}-GAL4	Bloomington Drosophila Stock Center	BDSC 458
UAS-TeTxLC.tnt G2	Bloomington Drosophila Stock Center	BDSC 28838
UAS-mLexA-VP16-NFAT, LexAop-rCD2-GFP (CaLexA)	Bloomington Drosophila Stock Center	BDSC 66542
LexAop-CD8-GFP-2A-CD8-GFP	Bloomington Drosophila Stock Center	BDSC 66545
iav-lexA::p65 (VK00013)	Bloomington Drosophila Stock Center	BDSC 52246
attP-9A (VK000013)	Bloomington Drosophila Stock Center	BDSC 9732
iav-GAL4.K	Bloomington Drosophila Stock Center	BDSC 52273
Software and algorithms		
FIMtrack	WWU Munster	http://www.uni-muenster.de/Informatik.AGRisse/media/fim-media.html
Fiji	ImageJ	http://imagej.net/software/fiji/
Python3.6	Python Software Foundation	https://www.python.org/
Prism_9	GraphPad	https://www.graphpad.com/
R	The R Project for Statistical Computing	https://www.r-project.org/
TREBLE	York et al.[18]	https://www.biorxiv.org/content/10.1101/2020.09.30.321406v2
PaSNA analysis	This paper	https://github.com/ClandininLab/pasna-acr-currbio2021

RESOURCE AVAILABILITY

Lead contact

Requests for information and resources not made available here should be directed to and will be fulfilled by the lead contact, Arnaldo Carreira-Rosario (arnaldo@stanford.edu).

Current Biology
Report

CellPress

Materials availability
This study did not generate new unique reagents.

Data and code availability
All original code for Figures 1, 2, and 3 has been deposited at https://github.com/ClandininLab/pasna-acr-currbio2021 and is publicly available as of the date of publication.

EXPERIMENTAL MODEL AND SUBJECT DETAILS

Drosophila Stocks
All stocks were kept at 25°C on molasses-based food. The following stocks were used: UAS-IVS-Syn21-GCaMP6s-P2A-nls-tdTomato-p10 on JK66B was a gift from Marta Zlatic (MRC Laboratory of Molecular Biology). LexAop- $Kir_{2.1}$ at VIE-260B, UAS-$Kir_{2.1}$ at VIE-260B and LexAop-TNT on VIE−260B were gifts from Barry Dickson (The University of Queensland). pBDP-LexA:p65 on attp40 was a gift from T. Shirangi (Villanova University). UAS-GtACR1 at attP2 was a gift from A. Claridge-Chang (Duke-NUS Med School). The following stocks were obtained from the Bloomington *Drosophila* Stock Center: elav-GAL4.L on 3rd (BDSC# 8760), elav-GAL4.L on 2nd (BDSC# 8765), GMR44H10-lexa::p65 on attP40 (BDSC# 61543), elav[c155]-GAL4 (BDSC# 458), UAS-TeTxLC.tnt G2 (BDSC# 28838), UAS-mLexA-VP16-NFAT, LexAop-rCD2-GFP (CaLexA) (BDSC# 66542), LexAop-CD8-GFP-2A-CD8-GFP on 2nd (BDSC# 66545), iav-lexA::p65[30] on VK00013 (BDSC# 52246), attP-9A VK000013 (BDSC# 9732) and iav-GAL4.K on 3rd (BDSC# 52273).

METHOD DETAILS

Embryo collection for calcium imaging
For all imaging experiments, embryos were collected in 15-30 min time windows the day before imaging, and grown at 25°C or 23°C on standard 3.0% agar molasses collection caps covered with a thin layer of wet yeast. Before imaging, embryos were dechorionated with double-sided tape and staged using elongation of the anterior midgut as a guide.[4,7] To prevent dehydration, embryos were transferred into Halocarbon oil or saline no more than 5 min after dechorionation.

Wide-field imaging
Staged, dechorionated embryos were mounted ventral side up on double-sided tape, covered with Halocarbon oil (180 cSt) and imaged using a Leica M205 FA system with a Plan Apo Corr. 2X objective. Stereoscopic magnification was used to achieve a final magnification of 64X. Fluorescent signals were acquired using LED illumination (CooLED pE-300 white). GCaMP6s was excited and collected using an ET470/40x ET525/50 m band-pass filter set, while tdTomato was excited and collected using an ET545/25x ET605/70 m band-pass filter set, acquiring each signal sequentially. Each cycle of imaging acquisition was 7 s long. We used a back-thinned sCMOS camera (Orca-Fusion BT - Hamamatsu) to capture images at a 1024 × 1024 resolution (after 2x2 binning), corresponding to a pixel size of 2.0 μm x 2.0 μm. Imaging sessions were up to 9 h in duration, depending on the experiment, and were conducted at 24 ± 1°C.

Two-photon imaging
Staged, dechorionated embryos were mounted ventral side up on Sylgard pads and imaged using a Bruker Ultima system. We used a Leica 20X HCX APO 1.0 NA water immersion objective lens, a piezo objective mount, resonant scanning and GaAsP PMTs. GCaMP6s and tdTomato signals were excited with a Chameleon Vision II laser (Coherent) at 920nm, and collected through a 525/50nm or a 595/50nm filter, respectively. Both signals were simultaneously collected using resonant scanning mode. Imaging volumes were acquired at an XY resolution of 358 × 148 (corresponding to a pixel size of 1.05 μm x 1.05 μm), with 41 z sections separated by 1.5 μm steps, at a volume rate of 2.6Hz. During the entire imaging session embryos were submerged in an oxygenated saline solution (as above), and kept at 25C°.

Immunostaining and confocal imaging
Immunostaining was performed as previously described.[31] The 1° antibody used was chicken anti-GFP (1:2,000, Abcam). The 2° antibody used was anti-chicken Alexa 488 (1:500, Life Technologies/Thermo Fisher). Confocal image stacks were acquired on a Leica SP8, using 40X HC PL APO 40X 1.3NA oil objective and a HyD detector. Images were processed in Fiji (https://imagej.net/Fiji). Adjustments to brightness and contrast were applied uniformly to the entire image.

Behavior data collection
Parents were crossed and fed with wet yeast containing 0.5 mM all *trans*-Retinal (ATR) at least three days before embryo collection. ATR and yeast were replaced every day. Embryos were collected for 30 min on standard 3.0% agar molasses collection caps covered with a thin layer of wet yeast without ATR and incubated at 25°C in darkness. 15.5 h later, embryos were placed under a 3.8uW/mm² 550nm LED for 5 h. Light pulses 600ms long were delivered at one second intervals, as previously shown to induce inhibition in *Drosophila* embryos using halorhodopsin.[23] Halorhodopsin, like GtACR1, is a silencing optogenetic tool that relies on

chloride ions entering the cell. Control animals were kept in the same incubator, in darkness. One day after light exposure was terminated, at the L1 stage, animals were collected and transferred to a Petri dish with 1.0% agar and relocated to a room kept at 23°C and 60% humidity. After 10 min of acclimation to the room, groups of 8 to 12 larvae were transferred to a 7.5 × 7.5 cm 1.0% agar arena. After 15 to 30 s, locomotion was recorded using a FIM imaging system[17] (https://www.uni-muenster.de/Informatik.AGRisse/media/fim-media.html) at 10 fps for 5 min. The FIM system was equipped with an azA2040-25 gm camera (Basler) and a TEC-V7X macro zoom lens (Computar). Individual larvae were then tracked using FIMtrack software.[17,32] Primary measurements from FIMtrack were used for behavioral analyses (see below).

QUANTIFICATION AND STATISTICAL ANALYSIS

Processing of calcium imaging data

After image acquisition, regions of interest (ROIs) were manually drawn on the ventral nerve cords and mean intensities were extracted using LAS X software (Leica Microsystems). For Figure 2 ROIs were drawn on Fiji (https://imagej.net/Fiji). To account for movement of the embryo and changes in gene expression over time, we encoded and recorded a structural fluorescent marker (tdTomato) in conjunction with the calcium sensor (GCaMP6s) and considered the ratio of the latter to the former as our measurement of calcium levels in the embryo. This ratiometric calcium signal was then converted into ΔF/F signal, dependent on a baseline signal computed separately for each embryo. For Figure 2, the initial baseline for ΔF/F prior to peak detection was determined by calculating the mean of the 100 values lowest ratiometric values. For Figures 1 and 3, the baseline for each time point in the ratiometric calcium signal was computed as a function of 16 min of the signal flanking the time point of interest (8 min prior to and 8 min after the time point). The 16-min signal was divided into 20 bins of signal amplitude ranges. The bin with the largest number of samples was taken to primarily reflect the baseline, while other bins were taken to reflect deviations from the baseline. The choice of 20 bins was made empirically based on the sparsity of neuronal activity. The mean of the samples in the largest bin was considered the baseline value for the time point in the middle. At the two edges of the signal, where the full 8 min prior to or after the considered time point do not exist, linear fits were used as the baseline. A 150 s, quartic Savitzky–Golay filter was applied to the resulting ΔF/F signal.

Episode and peak detection

For Figure 2, a 150 s, cubic Savitzky–Golay filter was first applied to the initial ΔF/F trace. Standard deviation for the filtered data was then calculated. Candidate first episodes were detected by finding the first instance where the filtered signal is equal to or greater than 1.2 times the standard deviation. Given that the intervals between episodes are at least 25 min, the large increase in signal must appear after a minimum of 30 min in order to be considered as a bona fide first episode. These candidate episodes were then manually curated for miss-called episodes due to small fluctuations that resulted in rapid increase in signal but were not sustained over longer than 20 s. Traces were then trimmed from −245 to 800 s (time series plots) relative to the initiation of the episode. These traces were used to calculate a new ΔF/F with a new baseline that was calculated as the mean of the 25 time points with the lowest signal. The Seaborn library was then used to plot traces.

For Figures 1 and 3, where episodes throughout PaSNA were monitored, peaks in the ΔF/F signal were detected using thresholds in the zeroth, first, and second derivatives of the signal. Each derivative signal was filtered with a 150 s, quartic Savitzky-Golay filter. The first derivative threshold was used to detect a rapid rise, while the second derivative was used to detect concavity. First, values crossing the zeroth derivative threshold were identified as peak candidates. A minimum peak distance of 500 s was enforced, following a greedy heuristic that kept candidates with the largest values first. Manually analyzed data showed that distinct episodes are invariably separated by more than 600 s. Then, of the remaining candidates, only those preceded by threshold crossings in both the first derivative and the second derivative within 210 s were kept and detected as episodes. Minimum thresholds of 0.06 for the zeroth derivative and 0.006 for the first derivative were derived empirically, while the maximum threshold of 0 for the second derivative was chosen to select for concavity. For Figures 3 and S2 we calculated the area under the curve 20 s surrounding the peak using the trapezoidal rule.

Stereotypy of episode timing

We assessed the extent to which PaSNA episodes occurred with stereotyped interpeak intervals by comparing the episode interval distributions of embryos to those generated under a null model. Under the null model, episodes corresponding to each real embryo occurred randomly following a Poisson process with a rate parameter equal to the mean rate of the first twelve episodes in the real embryo. In our Monte Carlo sampling of interpeak intervals, we rejected those under 500 s, consistent with the minimum peak distance imposed in our peak detection algorithm. We sampled 1,000,000 model embryos for each of 23 real embryos such that more than 500,000 remained after the rejections. We then computed the root mean squared error (RMSE) from the mean for each model dataset of 23 embryos, and the resulting distribution was compared against the RMSE computed for each peak in the real dataset. We assessed significance by examining how many model datasets had RMSE lower than that of each peak in the real dataset, and corrected for multiple comparisons using the Holm-Bonferroni method.

Statistical analysis

Statistical tests for Figures 3F, 3I, 3J, 3M, S2A, S2B, S2E, and S2H–S2J were done with Graphpad Prism. Statistical tests for Figures 3H, 3L, S2C, S2D, S2G, and S2K were done with scipy and statsmodels libraries. For two group comparisons with equal variance, we

Current Biology
Report

conducted unpaired Student's t test. For two group comparisons with unequal variance, we conducted Welch's t test. For three groups comparisons with unequal variance, we conducted Brown-Forsythe and Welch ANOVA followed by a Dunnett's T3 multiple comparison test. For multiple comparison of two groups we used an unpaired Student's t test with Holm-Bonferroni method.

Behavioral analysis

Primary measurements from FIMtrack[33] reflecting larval size, shape, and velocity were used for input, in addition to the angular velocity of the head, midpoint, and tail. Size measurements (i.e., area, perimeter, radii, spine length) were detrended using the ma function in the R package forecast (window size = 10) and converted to z-scores. Principal component analysis was used to control for potentially redundant information in the input features, yielding 8 principal components that explained > 90% of the variance in the feature set. To find the appropriate timescale with which to analyze the behavioral features an empirical window search procedure was used (described in[18]). We constructed behavior spaces using the top 8 PCs sweeping window sizes ranging between 100 ms and 5 s. For a given window size (denoted w), the windows were compiled as follows: given frame i, the 8 PCs corresponding to frames i:i+w were linearized and concatenated, resulting in a vector with length 8w. This was repeated for all windows in the dataset and the resulting vectors were appended to produce a window matrix with 8w rows. A behavior space was then constructed by embedding this matrix into low-dimensional space via the UMAP algorithm.[34] The appropriate window size was then determined by comparing the structural (Procrustes and Euclidean distance) and temporal features (recurrence) of behavior spaces produced from 20 random trials per window size. As was found before,[18] a window size of 800ms was chosen.

We then created a behavior space encompassing the full control and transient inhibition datasets using this window size. Trials were first filtered to include those that were longer than 2.5 s and that traveled at least 50mm, resulting in 84 control and 97 transient inhibition trials and a total of 179,409 frames. The resulting behavior space captured the major components of the larval foraging ethogram (Figures 4B and 4C). Differences in behavior patterns between the conditions were inferred using 2-dimensional kernel density estimation (as in Figures 4B and 4C) computed over all trials for each condition. The difference map in Figure 4F was produced by first normalizing via division by the greatest value (to produce a range of values between 0 and 1) and then subtracting the transient inhibition map from the control map. Differences in individual feature distributions (as in Figure 4G) were assessed using a Kruskal-Wallis test comparing the mean value for each trial across conditions (for each test n = 84 control and n = 97 for inhibited). To control for the autocorrelation in behavior we sampled each measurement every 10th frame for a total of ∼8,000 measurements per condition.

Louvain clustering was used to identify discrete components of behavior space. First, a graph was created with 2 sets of edges: the first representing the xy-coordinates in behavior space for each frame and the second corresponding to the xy-coordinates of the immediately following frame. This graph provides both information about the local neighborhood densities of the points in behavior space and the temporal sequencing between points over time. Louvain clustering was then run on this graph using the function cluster_louvain in the R package igraph.[35] Differences in occurrence in each cluster between the conditions were assessed using a Kruskal-Wallis test, again comparing the occurrence density of all individual trials between the two conditions (n = 84 control and n = 97 for inhibited).